



Thermal evolution of a metal drop falling in a less dense, more viscous fluidB. Qaddah ^{1,2,*}, J. Monteux,² and M. Le Bars ¹¹*CNRS, Aix Marseille Université, Centrale Marseille, IRPHE, 13013 Marseille, France*²*Université Clermont Auvergne, CNRS, IRD, OPGC, Laboratoire Magmas et Volcans, F-63000 Clermont-Ferrand, France*

(Received 20 December 2019; accepted 16 April 2020; published 15 May 2020)

The initial state of terrestrial planets was partly determined, during accretion, by the fall of metal drops in a liquid magma ocean. Here we perform systematic numerical simulations in two-dimensional cylindrical axisymmetric geometry of these falling dynamics and associated heat exchanges at the scale of one single drop for various initial sizes and ambient viscosities. We explore Reynolds number in the range 0.05–48, viscosity ratios in the range 50–4000, Weber number in the range 0.04–5, and Peclet number in the range 70–850. We show that heat exchange between the two phases occurs predominantly at the front section of the drop. Our systematic, parametric study shows that the thermal boundary layer thickness, the depth and time for equilibration, the Nusselt number, and the magma ocean volume affected by thermal exchanges all scale as power laws of the Peclet number. Because of drop distortions, these scaling laws deviate from the classical balances considering only heat diffusion through a laminar thermal boundary layer. Finally, when considering a temperature-dependent viscosity of the ambient fluid, we show that a low-viscosity layer surrounds the drop, which influences the thermal evolution of nondeformable, low-Reynolds-number drops only and decreases the breakup distance for some limited breakup modes.

DOI: [10.1103/PhysRevFluids.5.053801](https://doi.org/10.1103/PhysRevFluids.5.053801)**I. INTRODUCTION**

Core formation of terrestrial planets is a complex process contemporaneous with planetary accretion [1,2]. Its fluid dynamics and thermodynamics have been addressed in numerous studies (e.g., Refs. [3–8]). During the last stages of, e.g., Earth accretion, giant impacts likely occurred between the proto-Earth and up to Mars-sized differentiated bodies [9]. The kinetic energy released during such collisions [10,11], the radioactive heating caused by the disintegration of short-lived radio elements [12], and the heat dissipation resulting from the conversion of potential energy during core formation and core/mantle separation [13], melt part or all of the Earth mantle [11]. Following each impact, the iron core of the impactor thus spread and sank into a deep magma ocean. There, the metal further fragmented into blobs of different sizes, ranging from millimeter drops up to kilometer diapirs before assembling with the Earth protocore ([4,8,14,15]). Thermochemical exchanges occurred between the fragmented metal drops and the liquid magma ocean during their sinking, determining the initial thermal and chemical state of the planet ([4,16–18]). Past studies have provided many scenarios to characterize and quantify the thermochemical exchanges. References [17] and [19] modelled the diffusive equilibration through a laminar thermal boundary layer of, respectively, a cloud of uniform drops and a large diapir of iron. Reference [18] further evaluated the influence of drop deformations in Ref. [17]

*Corresponding author: qaddah@irphe.univ-mrs.fr

scenario. Reference [20] solved the fully coupled dynamical and thermal/chemical equations, but for a fixed spherical geometry only. Reference [4] used experiments where a large volume of immiscible fluid falls into a less dense ambient to show that the smallest scale of turbulence—rather than diffusion through a laminar boundary layer—leads to rapid thermochemical equilibration, even before fragmentation. Reference [7] confirmed this conclusion in their analog model, measuring the global cooling of a large volume of hot Galinstan after its fall through a deep tank of viscous oil. Yet a systematic temporal description of heat exchanges at the scale of one falling, freely evolving drop, is still missing.

Importantly, the magma ocean viscosity highly depends on its evolving temperature and pressure [21]. Therefore, the viscosity ratio between the magma ocean and iron drops can vary by several orders of magnitude as a function of depth, of time after impact, etc. Following and extending an abundant literature in different contexts (e.g., Refs. [22–26]), analog experiments in Refs. [7,8] and numerical simulations at the scale of one metal drop in Ref. [27] showed that the viscosity contrast indeed plays an important role in iron drops shape, velocity, and fragmentation. Reference [27] predicted that thermochemical exchanges should increase with drop deformation and oscillations; but they did not explicitly solve for the fully coupled dynamical and thermal equations. This is the purpose of the present paper. Open questions include the following: How and where do heat exchanges occur? Do the drop deformation/oscillations indeed favor heat exchanges? What are the characteristics time and depth needed to reach equilibration between the two phases? And what is the influence of a temperature-dependent viscosity of the magma?

The paper is organized as follows. Section II introduces the physical and numerical models, with the governing equations, the nondimensional parameters, and the numerical method. Section III presents in detail a reference case, describing its mechanical and thermal behavior, average temperature evolution, heat transfer at the drop interface, and the magma ocean volume heated during the drop sinking. In Sec. IV, we present the main numerical results from our systematic parametric study and derive generic scaling laws for the above detailed parameters. Section V then focuses on changes induced by a temperature-dependent viscosity in the magma ocean. Conclusions and future works are outlined in Sec. VI.

II. PHYSICAL AND NUMERICAL MODELS

A. Governing equations

We consider an initially spherical, liquid metal drop of radius R , falling in an initially motionless, less dense and more viscous surrounding fluid (i.e., a magma ocean) under the action of gravity. The initial temperature of the liquid drop and of the magma ocean strongly depends on the growth history of the protoplanet before the impact and on its initial heating caused by short lived elements [13]. Here we consider that the liquid metal drop is hotter than the magma ocean, with uniform initial temperatures in both phases. Both phases behave as Newtonian, incompressible, and immiscible fluids with uniform surface tension and constant density and viscosity within each fluid at first. In Sec. V, we also consider a temperature-dependent magma ocean viscosity. The dynamical and thermal evolution of the falling drop and ambient liquid is governed by the Navier-Stokes and heat transfer equations, describing

- (i) The mass conservation:

$$\nabla \cdot \mathbf{u} = 0, \quad (1)$$

with \mathbf{u} the fluid velocity vector (m s^{-1}).

- (ii) The momentum conservation:

$$\rho \left(\frac{\partial \mathbf{u}}{\partial t} + \mathbf{u} \cdot \nabla \mathbf{u} \right) = \nabla \cdot \left\{ -P\mathbf{I} + \mu[\nabla \mathbf{u} + (\nabla \mathbf{u})^T] \right\} + \rho \mathbf{g} + \mathbf{F}_{\text{st}}, \quad (2)$$

with ρ the fluid density (kg m^{-3}), μ the fluid dynamic viscosity (Pa s), t the time (s), P the fluid pressure (Pa), \mathbf{g} the gravitational acceleration (m s^{-2}), \mathbf{F}_{st} the surface tension force (N m^{-3}) and \mathbf{I} the identity matrix.

(iii) The heat conservation:

$$\rho C_p \left[\frac{\partial T}{\partial t} + \mathbf{u} \cdot \nabla T \right] + \nabla \cdot [-k \nabla T] = 0, \quad (3)$$

with C_p the heat capacity at constant pressure ($\text{J kg}^{-1} \text{K}^{-1}$), T the fluid temperature (K), and k the fluid thermal conductivity ($\text{W m}^{-1} \text{K}^{-1}$). No heat source is considered in our model. In this work, we ignore the effect of viscous heating. Viscous heating during km-scale metal diapir sinking can significantly increase the temperature of the diapir and of the surrounding material depending on the viscosity contrast between the metal and silicate phases [13,28]. When considering the full mantle/core separation within terrestrial planets, viscous heating should be accounted for in the heat budget [29]. In this study we focus on small droplets (millimeters to centimeters in radius) falling over short distances (up to 200 times their radius). Our results (not shown here) confirm that thermal contribution from viscous heating is negligible at such small scales.

To monitor the interface between the falling drop and the magma ocean, we use the level set method, a Eulerian and implicit method frequently used in multiphase flow problems (e.g., Ref. [30]). The level set function ϕ equals to 1 in the metal drop and 0 in the ambient liquid and rapidly changes through the interface, whose position is determined by the isocontour $\phi = 0.5$. The transport and reinitialization of the level set function ϕ are governed by:

$$\frac{\partial \phi}{\partial t} + \mathbf{u} \cdot \nabla \phi = \gamma \nabla \cdot \left[\epsilon \nabla \phi - \phi(1 - \phi) \frac{\nabla \phi}{|\nabla \phi|} \right], \quad (4)$$

with γ (m/s) and ϵ (m) the reinitialization parameters. γ determines the reinitialization amount: A suitable value for γ is the maximum velocity magnitude experienced in the model. ϵ determines the layer thickness around the interface and is equal to half the size of the characteristic mesh in the region explored by the interface. The density and dynamical viscosity are evaluated using the level set function:

$$\rho = \rho_m + (\rho_d - \rho_m)\phi, \quad (5)$$

$$\mu = \mu_m + (\mu_d - \mu_m)\phi, \quad (6)$$

where subscripts “m” and “d” denote the magma ocean and the liquid metal drop, respectively. The surface tension force is determined by:

$$\mathbf{F}_{\text{st}} = \nabla \cdot \mathbf{T} = \nabla \cdot \{\sigma [\mathbf{I} + (-\mathbf{nn}^T)] \delta\}, \quad (7)$$

with σ (N/m) the surface tension coefficient, \mathbf{I} the identity matrix, \mathbf{n} the interface normal unit vector, and δ the Dirac δ function, nonzero only at the fluid interface. The interface normal unit vector is calculated as

$$\mathbf{n} = \frac{\nabla \phi}{|\nabla \phi|}. \quad (8)$$

The level set parameter ϕ is also used to approximate the δ function by a smooth function [31] defined by

$$\delta = 6 |\phi(1 - \phi)| |\nabla \phi|. \quad (9)$$

Note that in this work, we focus on thermal exchanges only and do not calculate the chemical exchanges between the two phases, which are also extremely interesting from a geological point of view (see, e.g., Ref. [32]). Indeed, the main difficulties in solving for chemical exchanges are (i) the small value of the chemical diffusivities and (ii) the presence of a partition coefficient at the

TABLE I. Symbol definitions and values of the physical and nondimensional parameters used in this study.

	Symbol	Value or range
Magma ocean density	ρ_m	3500 kg m ⁻³
Metal drop density	ρ_d	7500 kg m ⁻³
Metal drop viscosity	μ_d	0.005 Pa s
Magma ocean viscosity	μ_m	0.25–20 Pa s
Initial drop radius	R	4–25 mm
Surface tension coefficient	σ	1 N m ⁻¹
Magma ocean heat capacity	Cp_m	667 J kg ⁻¹ K ⁻¹
Metal heat capacity	Cp_d	800 J kg ⁻¹ K ⁻¹
Magma ocean conductivity	k_m	10 W m ⁻¹ K ⁻¹
Metal conductivity	k_d	100 W m ⁻¹ K ⁻¹
Viscosity ratio	R_μ	50–4000
Density ratio	R_ρ	2.14
Reynolds number	Re	0.05–48
Weber number	We	0.04–5
Peclet number	Pe	70–850
Nusselt number	Nu	1–6

metal/magma interface, meaning that species concentration at the moving interface is discontinuous [32]. Such challenges are at present beyond the scope of our numerical study. We nevertheless argue that the main conclusions shown here for heat exchanges also give some clues for chemical exchanges and hence should be accounted for in geochemical models of planet building [33].

B. Physical and nondimensional parameters

The main parameters that characterize the dynamical and thermal evolution of a falling drop in a more viscous medium are the viscosity, density, thermal conductivity, heat capacity, and initial temperature of the two fluids; the initial drop size; the gravity; and the surface tension between the two phases. In the geophysical problem of interest (i.e., core formation), the magma ocean viscosity and the metal drop initial radius vary over a wide range of values, while the other parameters are roughly constant (even if rigorously, the thermal conductivity and heat capacity of a magma ocean moderately depend on its composition (e.g., Refs. [34,35]), and the thermal conductivity and heat capacity of metal drops moderately depend on temperature and pressure (e.g., Refs. [36,37])). Hence in this study, we vary these two parameters R and μ_m , in the accessible, relevant ranges 4–25 mm and 0.25–20 Pa s, respectively, while we keep all the other parameters fixed at their representative geophysical values (see Table I).

In our simulations, the drop falls from rest, accelerates until reaching a constant terminal velocity, possibly with small oscillations around it, and exchanges heat with the ambient liquid. We continue our simulations until the drop reaches a stable dynamical regime and its temperature contrast with the ambient reaches less than 20% of its initial value. During the fall, we monitor the average velocity V and the average temperature T of the drop (minus the initial ambient temperature). The dynamical and thermal evolution of each drop is then characterized by the following output dimensionless numbers, where we use the terminal average velocity (note that if it has not yet reached a steady value by the end of the computation, we use estimate from our previous study [27]):

(i) The Reynolds number ($\text{Re} = \frac{\rho_m V R}{\mu_m}$) is the ratio of inertial to viscous forces. Three different regimes are possible: The Stokes regime corresponds to $\text{Re} < 1$ where the viscous effects dominate; the intermediate regime corresponds to $\text{Re} = 1 - 500$ where both viscous and inertial forces are important; and the Newtonian regime corresponds to $\text{Re} > 500$ where the inertial forces are

TABLE II. Dimensional and nondimensional parameters for all performed simulations used in this study. Pe_h is the grid Peclet number (see Sec. II C).

Simulation	R (mm)	μ_m (Pa s)	R_μ	Re	We	Pe	Pe_h	ΔT (K)
no. 1	8	20	4000	0.05	0.04	70	0.43	100
no. 2	8	10	2000	0.2	0.15	137.26	0.84	100
no. 3	8	5	1000	0.76	0.52	254	1.55	100
no. 3a (T -dependent μ_m)	8	5	1000	0.81	0.59	271	1.65	100
no. 3b (T -dependent μ_m)	8	5	1000	0.98	0.85	327	2	1000
no. 4	8	1	200	9.5	3.23	635	3.89	100
no. 5	8	0.5	100	21.8	4.26	728.36	4.46	100
no. 5a (T -dependent μ_m)	8	0.5	100	22.4	4.48	747.6	4.57	100
no. 5b (T -dependent μ_m)	8	0.5	100	23.52	4.94	785	4.8	1000
no. 6	8	0.25	50	47.6	5	793.73	4.86	100
no. 6a (T -dependent μ_m)	8	0.25	50	47.6	5	793.73	4.86	100
no. 6b (T -dependent μ_m)	8	0.25	50	47.6	5	793.73	4.86	1000
no. 7	4	1	200	2.2	0.34	145.67	0.89	100
no. 8	6	1	200	5.67	1.53	378.19	2.32	100
no. 9	10	1	200	12.7	4.61	847.42	5.2	100
no. 10	25	1	200	45	23.2	3008	18.45	100
no. 10a (T -dependent μ_m)	25	1	200	41.13	19.5	2745	16.8	1000

dominant. Here the Reynolds number ranges from 0.05 to 48, and hence our drops are in the Stokes to intermediate regimes.

(ii) The Weber number ($We = \frac{\rho_m V^2 R}{\sigma}$) compares the inertial and surface tension forces. It governs the deformation, breakup, and terminal shape of a drop (see, e.g., Refs. [27,38]). When $We < O(1)$, the drop remains spherical without any change of its morphology, while increasing Weber number leads to stronger and stronger deformation, then to fragmentation above a threshold which increases with the viscosity ratio, starting from ~ 3 for viscosity ratio ≤ 1 (see, e.g., Refs. [27,39]). Here the Weber number ranges from 0.04 to 5, considering stable, potentially deformable drops only.

(iii) The Peclet number ($Pe = \frac{\rho_m C_p V R}{k_m}$) compares the rate of heat advection to diffusion at the drop scale. Here the Peclet number ranges from 70 to 850, so heat transfer is strongly affected by advection.

(iv) The Nusselt number [$Nu = \frac{R \nabla T \cdot \mathbf{n}}{(T_{\text{int}} - T_m)}$] compares the measured, averaged heat transfer at the drop interface to a purely conductive case, with $\overline{T_{\text{int}}}$ the mean temperature at the interface and T_m the magma ocean temperature far from the drop. Here the Nusselt number ranges from 1 to 6, hence confirming the important role of advection in heat transfer.

All relevant parameter values are given in Table I.

C. Numerical model

We solve Eqs. (1)–(4) using axisymmetric simulations with COMSOL Multiphysics software, based on the finite-element method. The details of our 17 runs for this study are listed in Table II. Each run represents 2 to 4 weeks' computation time on a biprocessor, eight-core, 3.2- to 3.6-GHz workstation. The axisymmetric geometry assumption is validated in Ref. [40] for a Weber number up to 120. For the dynamics, we use open conditions at the top and bottom boundaries and no-slip conditions at the lateral boundary. For the temperature, we consider no flux conditions at all boundaries. The computational domain must be large enough to allow for convergence without any wall effects. Here we chose an axisymmetric cylinder of size $(r \times z) = (12R \times 200R)$, which is sufficiently large to reach a statistically steady motion (see our previous study [27]) and to follow equilibration up to a 80% decrease of the initial temperature anomaly.

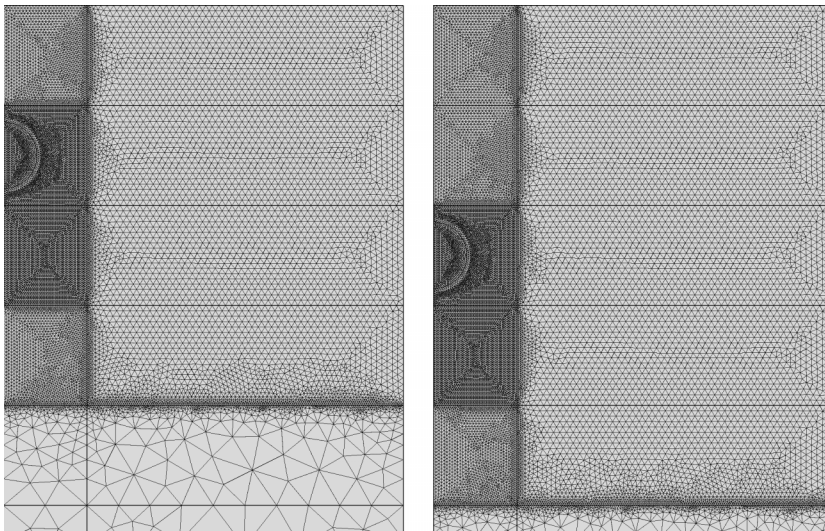


FIG. 1. A zoom illustrating our adaptive mesh (left) and the method for mesh evolution over time when the drop reaches the bottom of the finest mesh region (right).

To capture precisely the dynamical and thermal evolution of the drop, a fine mesh is required. For that, we use an adaptive mesh with a high resolution in the drop vicinity. As shown in Fig. 1, we divide our domain into several regions where the cell sizes vary between $h = 0.015R$ and $h = 1.5R$. As detailed in Ref. [27], the simulation is programmed to stop when the drop reaches the bottom of the finest mesh region: The whole mesh pattern is then translated and the simulation is restarted on this new grid [see Fig. 1 (right)].

Mesh convergence has been checked, always using standard Lagrange mesh elements of type P2-P3 (quadratic for the pressure and temperature fields and cubic for the velocity field). In Ref. [27], we showed that a mesh size $h = 0.025R$ (or smaller) allows us to capture the falling drop dynamics. Here we further performed two tests for the resolution of thermal transfers. In the first one, we compare the numerical and analytical heat transfers by thermal diffusion from a motionless spherical drop. The analytical solution for the radial temperature profile from the drop center to a given distance (r) is given by [41]

$$T = 0.5T_0 \left[\operatorname{erf} \frac{R+r}{2\sqrt{Dt}} + \operatorname{erf} \frac{R-r}{2\sqrt{Dt}} \right] - \frac{T_0}{r} \sqrt{\frac{Dt}{\pi}} \left[e^{-\frac{(R-r)^2}{4Dt}} - e^{-\frac{(R+r)^2}{4Dt}} \right] \quad (10)$$

with T the temperature anomaly (T_0 its initial value) and D the thermal diffusivity ($m^2 \text{ s}^{-1}$). Figure 2 (left) shows the excellent agreement of our numerical results.

For the second test, we calculated, for different minimum grid sizes $h = 0.05R, 0.035R, 0.025R, 0.015R, 0.01R$, the normalized average drop temperature as a function of normalized time for our reference case no. 4 in Table II (see details in next section). Figure 2 (right) shows a reasonable convergence of the numerical results from $h = 0.015R$, with a relative maximum error $\simeq 3.5\%$, while the drop mass during the course of this simulation does not change by more than 0.4% from its initial mass. Therefore, we confirm that our mesh $h = 0.015R$ captures correctly the thermal evolution of the metal drop.

Finally, the grid Peclet number $\text{Pe}_h = \frac{Vh}{D_{\text{int}}}$, with $D_{\text{int}} = \frac{D_d + D_m}{2}$ the mean thermal diffusivity, is an appropriate parameter in the convection-diffusion equation to determine whether the heat transfer in the system corresponds to numerical artifacts or not. Reference [42] found very accurate solutions for grid Peclet number up to 10. As shown in Table II, our runs in this study remain below this

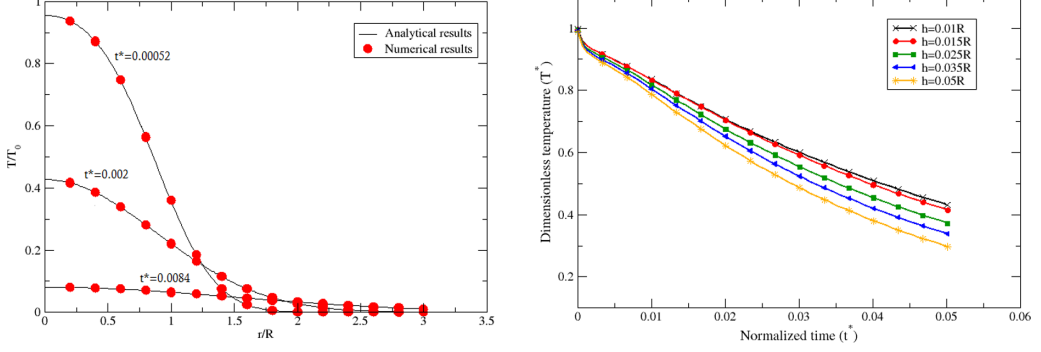


FIG. 2. Left: Comparison of our numerical results with the analytical results in Ref. [41] for the radial profile of the normalized temperature anomaly for a nondeformable and immobile drop. Right: Comparison of the time evolution of the normalized mean temperature anomaly determined with different mesh sizes for a deformable and mobile drop (simulation no. 4 in Table II).

criterion for stability, except for run no. 10, which we hence do not consider for heat transfer studies in the following sections.

III. REFERENCE CASE

In this section, we present our reference case, from which, in the next section, we then change the drop size keeping the viscosity ratio constant, and the magma ocean viscosity keeping the drop size constant. This reference case corresponds to simulation no. 4 in Table II: The drop initial radius is 8 mm, the magma ocean viscosity is 1 Pa s, the metal viscosity is 0.005 Pa s (viscosity contrast 200), and the initial temperature difference between the metal drop and the magma ocean is 100 K.

The drop motion from rest and its thermal evolution are shown in Fig. 3. The spherical drop accelerates due to gravity and rapidly deforms into a spherical cap. Then, surface tension equilibrates inertia at the drop interface and prevents any further change in morphology. Higher temperatures are concentrated at the front of the drop, while the thermal wake behind the drop expands as a function of time. To characterize this dynamics, we define and compute the following quantities.

A. Average drop velocity

During its fall, the drop mean velocity varies with time depending on the drop morphology. In our simulations, we compute it as:

$$V(t) = \frac{\int_v U(r, z, t) [\phi(r, z, t) \geq 0.5] dv}{\int_v [\phi(r, z, t) \geq 0.5] dv}, \quad (11)$$

with $U(r, z, t)$ the local velocity magnitude (m/s), $dv = 2\pi r dr dz$ accounting for axisymmetric cylindrical geometry, and $[\phi(r, z, t) \geq 0.5]$ the Boolean operator allowing to only capture the iron drop volume. Note that we use the mean magnitude velocity of the drop, which is actually very close to its average falling velocity (change of less than 3% in our reference case) because vertical motions largely predominate. We normalize $V(t)$ by the free fall Newton velocity $U_N = \sqrt{\frac{\Delta \rho g R}{\rho_m}}$ and time by the diffusion time $t_{\text{dif}} = \frac{R^2 \rho_m C p_m}{k_m}$. Figure 4 shows the result for our reference case. The drop rapidly accelerates from rest up to $t^* = 0.02$, then several small oscillations occur before converging toward its asymptotic terminal fall velocity, which we use to compute the output dimensionless numbers.



FIG. 3. Dynamical and thermal evolutions of the metal drop as a function of time for simulation no. 4 in Table II. The color presents the temperature anomaly normalized by its initial value T^* . The black solid line separates the metallic material from the magma ocean. From left to right, the time normalized by the thermal diffusion time is $t^* = 0, 0.01, 0.02, \text{ and } 0.05$.

B. Average temperature evolution of the metal drop

As shown in Fig. 3, the liquid drop exchanges heat with the liquid magma ocean and loses its heat as a function of time and depth. We determine the mean average temperature anomaly of the drop compared to the magma ocean as:

$$T(t) = \frac{\int_v T(r, z, t)[\phi \geq 0.5]dv}{\int_v [\phi \geq 0.5]dv}. \quad (12)$$

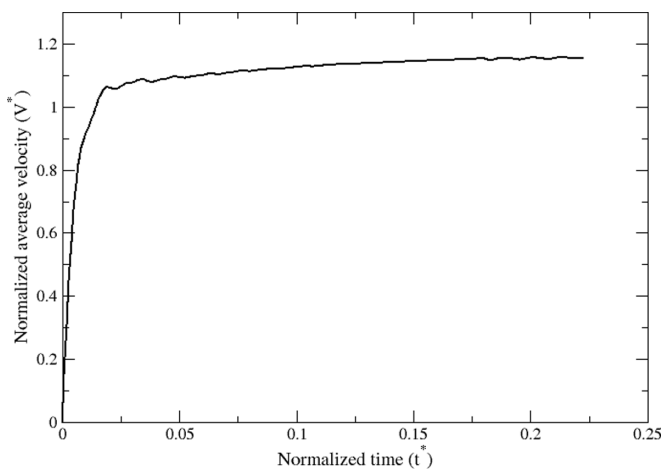


FIG. 4. Normalized average velocity of the metal drop as a function of normalized time for simulation no. 4 in Table II.

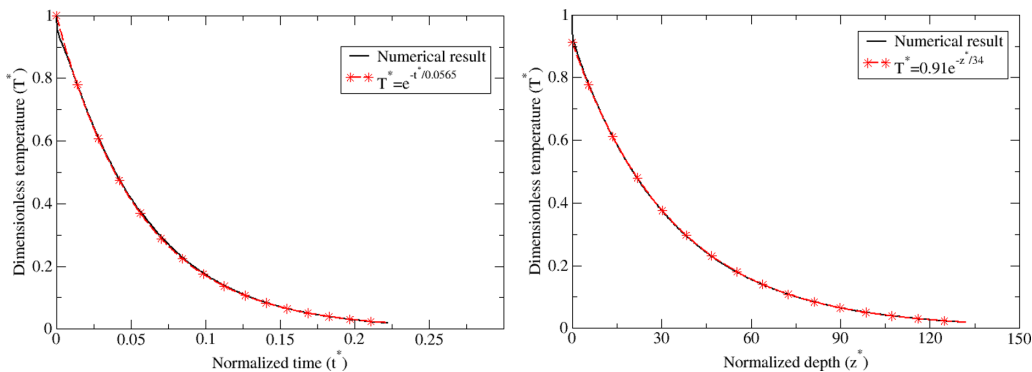


FIG. 5. Normalized average temperature anomaly of the metal drop as a function of normalized time (left) and depth (right) for simulation no. 4 in Table II. The black lines represent our numerical results and the red dashed lines with stars represent the exponential fits from Eq. (13). The correlation coefficient for the two fits is 0.9999.

We normalize $T(t)$ by its initial value, giving $T^*(t)$. Its evolution for the reference case as a function of time or as a function of depth of its center of mass (normalized by the initial radius R) is shown in Fig. 5. After a rapid adjustment of the initial temperature jump at the interface, T^* decreases exponentially toward equilibrium. We determine the best exponential fits according to

$$T^* = e^{(-t/t_c)} \quad \text{and} \quad T^* = C_z e^{(-z/l_c)}, \quad (13)$$

where C_z is a constant (see Fig. 5 in red with stars). In geophysical science, the characteristic time (t_c) and length (l_c) for equilibration are very important parameters [7], used to set the degree of equilibration between iron and silicate of magma ocean in planet building models [33]. Note that chemical equilibrium is more difficult to reach than thermal equilibrium because of the lower value of the chemical diffusivity. The chemical equilibration between the metallic phase and the magma ocean is a key process and constraints on this dynamics contribute to our understanding of the core formation in terms of timing. However, it is also a process that is complicated to compute because of the presence of a partition coefficient at the interface. The results shown below for thermal equilibrium may be considered as first-order trends for chemical equilibrium that will nevertheless deserve a dedicated study.

C. Volume of heated magma during the drop sinking

The magma ocean temperature increases during the fall of the drop, especially in its wake. It is important in geophysics to quantify how much of the magma is contaminated (here, thermally affected) by the formation of the iron core: This would for instance affect the initial structure and heat budget of the Earth's mantle. In our simulations, we calculate the volume of magma ocean affected by thermal exchange as:

$$V_0 = \int_v [T > T_C][\phi \leq 0.5] dv, \quad (14)$$

with T_C a chosen temperature anomaly (K) and $[\phi \leq 0.5]$ the Boolean operator allowing to only capture the magma ocean volume. An example of the captured volume of heated magma ocean is shown in Figure 6 (left). We performed tests with several T_C corresponding to 0.1, 1, and 10 K. Results of the volume normalized by the initial drop volume as a function of the drop depth are shown in Figure 6 (right). The three curves corresponding to different equilibrium degrees are parallel, until a depth equals to $50R$ where $T_C = 10$ K is strongly affected by thermal diffusion in the magma ocean. The same behavior would of course take place at longer time/depth for the

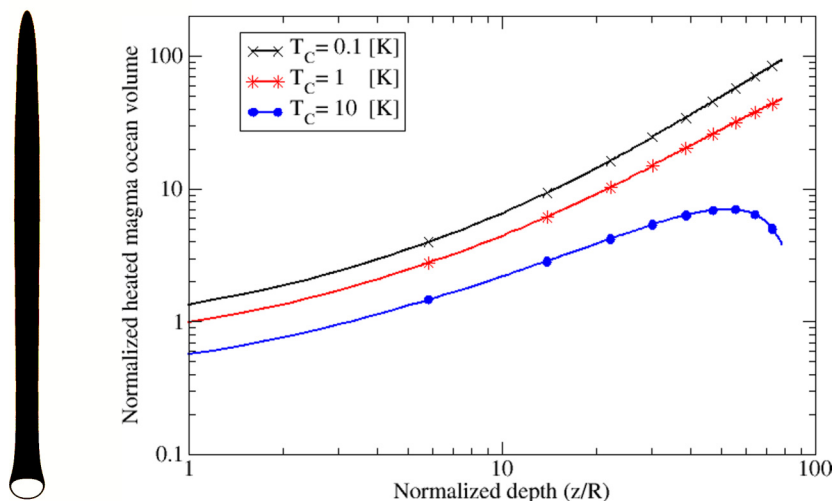


FIG. 6. Left: Volume of heated magma ocean ($T_C = 1$ K) once the drop reaches a time $t^* = 0.067$ and a depth $z = 37R$ in our simulation no. 4 in Table II. Right: Normalized heated magma volume as a function of normalized depth for different values of T_C .

other T_C . But our purpose here is to look at the relative initial behavior before the diffusion effect dominates, depending on the drop radius and magma viscosity. In the following, for our parametric study, we thus compare heated volumes considering $T_C = 1$ K at three different depths: $10R$, $20R$, and $30R$.

D. Heat transfer at the drop interface

To evaluate the Nusselt number, we compute the mean temperature anomaly and the mean temperature gradient at the interface, using, respectively,

$$\overline{T_{\text{int}}} = \frac{\int_v T \phi (1 - \phi) dv}{\int_v \phi (1 - \phi) dv}, \quad (15)$$

$$\overline{\nabla T_{\text{int}}} = \frac{\int_v \nabla T \phi (1 - \phi) dv}{\int_v \phi (1 - \phi) dv}, \quad (16)$$

where $\phi(1 - \phi)$ allows us to capture only the interface region between the two phases. Figure 7 shows the temperature gradient in and around the drop at a given time for our reference simulation. Most heat transfer between the metal drop and the magma ocean occurs at the drop front side, while the back half only accounts for about 15% of the total. The existence of a hot thermal wake and the external recirculation behind the drop that encapsulates and entrains magma with the sinking drop are the main reasons limiting back thermal exchanges [27,43].

A close view of the temperature field and of the thermal boundary layer is shown in Fig. 8. We define the thermal boundary layer thickness as the distance from the drop interface to a point where the temperature anomaly reaches 1% of its interfacial value. The boundary layer is very thin at the drop front section, where most thermal exchanges are carried out. It significantly increases behind the drop. An example of thickness measurement is shown in Fig. 8 (right) at the thinnest position, i.e., at the front of the drop. In order to give a global estimate around the drop, we also define the average boundary layer thickness as

$$\delta_{T_{\text{av}}} = \frac{\overline{T_{\text{int}}}}{\overline{\nabla T_{\text{int}}}}. \quad (17)$$



FIG. 7. Temperature gradient (K/m) in and around the drop for our reference simulation no. 4 in Table II at time $t^* = 0.055$.

IV. PARAMETRIC STUDY AND SCALING ANALYSIS

We now present our systematic exploration of the parameter space, changing the magma ocean viscosity or the drop initial radius as shown in Table II, from our reference simulation no. 4. We then analyze our results in terms of scaling laws. In particular we determine the influence of the Peclet number on the dimensionless parameters defined in the previous section: the time and length of equilibration, the normalized thermal boundary layer thickness, the Nusselt number, and the dimensionless magma ocean volume affected by thermal exchanges.

A. Time and length of equilibration

As expected from previous studies of drop dynamics, but largely neglected in geophysical applications (see, e.g., discussions in Refs. [8,27]), the characteristic time and length of equilibrium depend on the viscosity contrast between the metal drop and the magma ocean. As presented in Fig. 9, increasing the viscosity ratio increases the required time for thermal equilibration (Fig. 9,

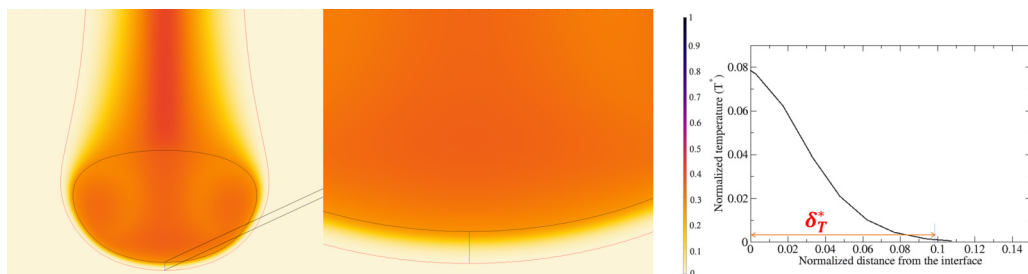


FIG. 8. Left: Temperature anomaly (color scale) and contour of the thermal boundary layer (red line) around the drop (black line) for our reference simulation no. 4 in Table II at time $t^* = 0.067$. Middle: zoom at the drop front. Right: Temperature profile of the thermal boundary layer in front of the drop and determination of the local boundary layer thickness.

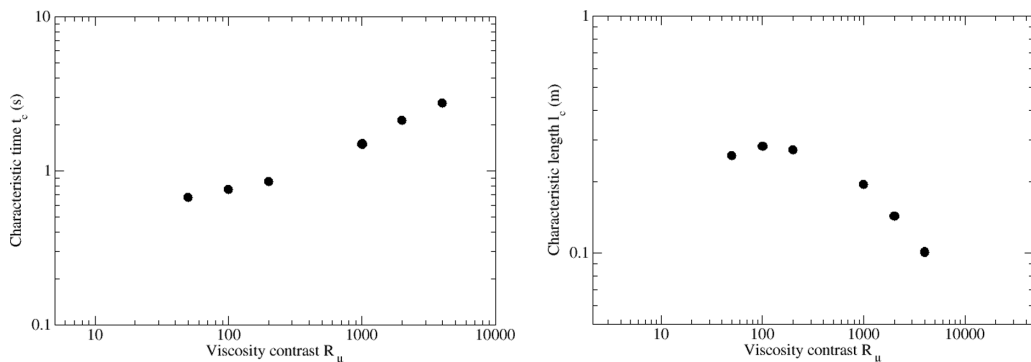


FIG. 9. Characteristic time (left) and length (right) of equilibration as a function of the viscosity contrast [see Eq. (13)].

left), mostly because a larger ambient viscosity limits advective heat exchanges. We can further observe in Fig. 9 (left) two different slopes corresponding to two different dynamical regimes of the drop: For $R_\mu > 1000$, the drop remains spherical and the equilibration characteristic time is highly dependent on the viscosity ratio, while for $R_\mu < 200$, the drop deforms which limits the influence of R_μ . The evolution of the equilibration length is nonmonotonic (Fig. 9, right), because the magma ocean viscosity also influences the falling velocity. Globally, with a more viscous ambient fluid, the thermal equilibrium between the two phases occurs less deeply in the magma ocean once the stable drop is formed, as we predicted in our previous work [27].

The drop size at a given viscosity ratio also influences the thermochemical equilibration (for a fixed spherical shape, see Ref. [20]). Increasing the initial radius of the liquid metal drop decreases the surface of exchange over volume initial ratio and increases the drop falling velocity: We thus expect an increase of both the characteristic time and length, as confirmed in Fig. 10. In Ref. [27], we predicted that increasing the drop initial radius also leads to surface extension due to drop distortion, hence to faster equilibration compared to a purely spherical drop: This effect is, however, limited, because drop deformation mostly occurs at the back of the drop, while heat exchange takes place mostly at the front.

Those two series of results can be rationalized by considering dimensionless properties as a function of the Peclet number. Here we normalize the equilibrium time by the thermal diffusion time and the equilibrium length by the initial drop radius. Results are shown in Fig. 11. The thermal equilibrium time for a high Peclet, spherical drop theoretically scales as $Pe^{-0.5}$ (see, e.g., Ref. [32]).

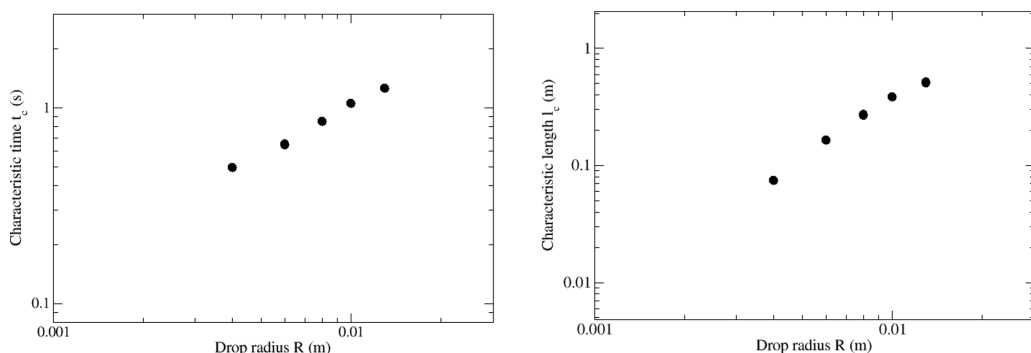


FIG. 10. Characteristic time (left) and length (right) of equilibration as a function of the drop initial radius [see Eq. (13)].

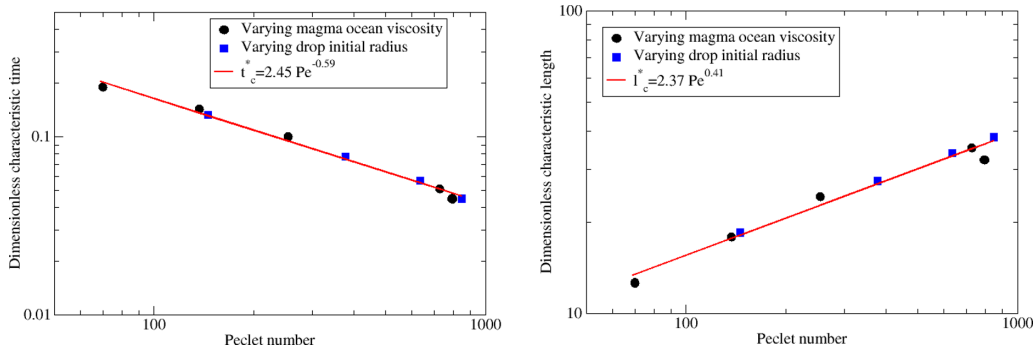


FIG. 11. Dimensionless equilibrium time (left) and length (right) as a function of the Peclet number.

Here we find

$$t_c^* = 2.45\text{Pe}^{-0.59 \pm 0.01}, \quad (18)$$

where the shown uncertainty in the exponent comes from considering separately numerical simulations performed while changing the viscosity ratio and those performed while changing the initial sphere radius. This acceleration of the equilibration compared to the theoretical model may be a signature of the drop deformation at large Peclet. Indeed, performing the same fit only on the subset of data points where the drop remains spherical gives an exponent 0.51 ± 0.01 .

Correspondingly, the length needed to reach the equilibration increases monotonically with Peclet number following

$$l_c^* = 2.37\text{Pe}^{0.41 \pm 0.01}, \quad (19)$$

in agreement with a quasiconstant falling velocity, i.e., $l_c = V \times t_c$. In conclusion, when the flow advection measured by the Peclet number increases, thermal equilibration occurs faster but deeper in the magma ocean (after drop formation), which is of importance for Earth's building models [33].

B. Heat exchanges

Simply equilibrating large-scale heat advection along the drop surface with heat diffusion through the thermal boundary layer perpendicular to it, the theoretical size of the thermal boundary layer normalized by the drop radius classically scales as $\text{Pe}^{-0.5}$: This was verified numerically in Ref. [20] for a rigid falling sphere. As shown in Fig. 12 (left), we also recover this scaling at the drop front, where most heat exchange occurs: The best fit gives

$$\delta_T^* = 2.53\text{Pe}^{-0.5 \pm 0.01}. \quad (20)$$

With the deformable drops considered here, however, the boundary layer thickness strongly varies around the metal drop: We thus compute a characteristic average value $\delta_{T_{\text{av}}}^*$ from Eq. (17), normalized by the initial radius. Results are shown in Fig. 12 (right), with the best-fit scaling law

$$\delta_{T_{\text{av}}}^* = 10.7\text{Pe}^{-0.6 \pm 0.01}. \quad (21)$$

Over the explored range, the average thickness is at least three times larger than the front one. The larger-than-expected 0.6 exponent might again be a signature of drop distortion at large Peclet number.

Then, by definition, the Nusselt number averaged over the drop surface should scale as $1/\delta_{T_{\text{av}}}^*$. This is indeed recovered, as shown in Fig. 13 with the best-fit scaling law

$$\text{Nu} = 0.08\text{Pe}^{0.63 \pm 0.02}. \quad (22)$$

Note that Nu varies over time in many cases in this study: We consider here its time-averaged value.

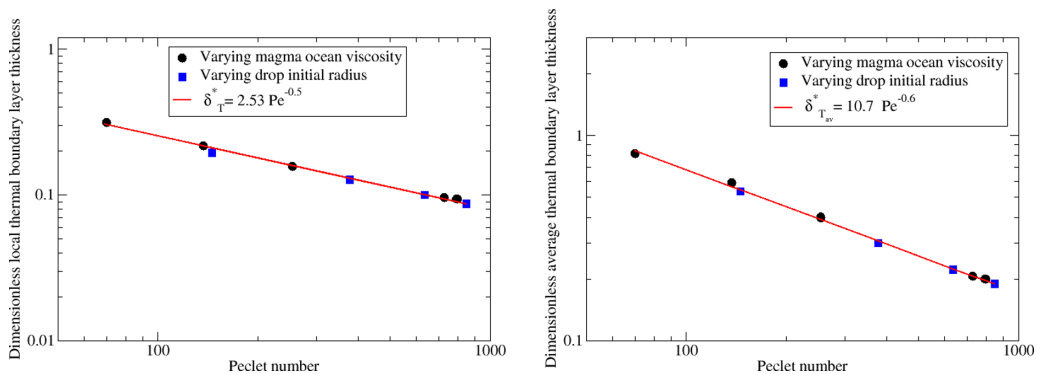


FIG. 12. Dimensionless thickness of the thermal boundary layer at the drop front as a function of Peclet number (left). Dimensionless average thickness of the thermal boundary layer around the drop as a function of Peclet number (right).

Comparing this result with the one obtained in the previous section, we also recover that the typical dimensionless time for equilibration t_c^* scales like $1/\text{Nu}$, as expected. This proves the self-consistency of our measurements.

C. Volume of heated magma ocean

In the wake of the drop, the magma ocean is thermally affected by its passage. Because of heat diffusion within the magma ocean, the affected volume widens with time. But on the short times, at a given depth of the drop z , it can be estimated by simply balancing the heat that has passed through the drop interface with the heat accumulated in this volume of magma ocean, whose temperature has increased by a given amount larger or equal to T_C . We then predict

$$\text{Vo}^* = \frac{\text{Volume of heated magma}}{\text{Initial drop volume}} \sim 3 \frac{\text{Nu } z \Delta T_0}{\text{Pe } R T_C}, \quad (23)$$

with ΔT_0 the initial temperature difference between the two phases. Results in Fig. 14 show a good agreement with a small relative error for various depths $z = 10R, 20R, 30R$ and temperature

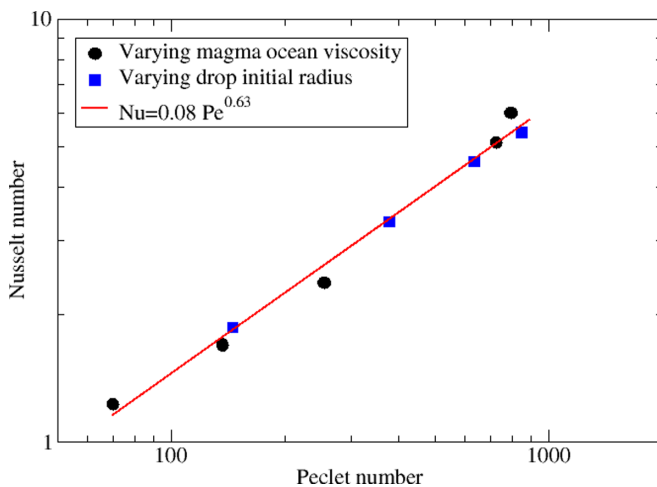


FIG. 13. Nusselt number as a function of Peclet number

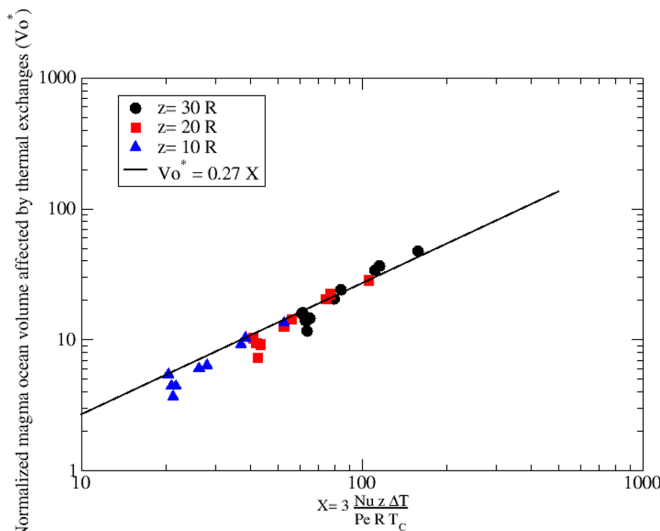


FIG. 14. Dimensionless heated magma ocean volume as a function of X , and comparison with our scaling law (23). Our numerical results are represented with different symbols for different given depths.

contrast $T_C = 1K$, using the previously determined scaling for Nu . This volume can be compared to the volume crossed by the falling drop, which writes in its dimensionless form

$$V_{\text{crossed}}^* = \frac{\pi R^2 z}{4/3\pi R^3} = \frac{3z}{4R}, \quad (24)$$

which also scales linearly with depth. Our result does not exhibit any strong increase of the volume effectively contaminated vs. this simple geometrical estimate: this is because, even in our most turbulent cases, the falling drop encapsulates in its wake a small volume of silicate and entrains it toward the deep, while the rest of the ambient fluid remains largely motionless or laminar. No additional mixing is generated. Our conclusion should nevertheless be re-evaluated in the presence of global magma motions, coming, e.g., from turbulent convection, depending on the typical excited time- and length scales. But this is beyond the scope of the present paper. Our conclusion should also be re-evaluated while considering large-scale viscous heating which, for a turbulent wake of a large diapir or a large cloud of drops, might generate strong additional heating long after the iron fall.

V. INFLUENCE OF A TEMPERATURE-DEPENDENT VISCOSITY

The magma ocean viscosity increases from the surface to the base of the magma ocean because of the combined effects of temperature and pressure [21]. Those large-scale variations are irrelevant in the context of our local study; nevertheless, during the drop fall over the typical length of $\sim 200R$ considered here, the temperature of the liquid magma ocean increases because of heat exchanges with the drop, therefore its viscosity decreases at a given pressure (i.e., depth) following the equation in Ref. [21] for anhydrous liquid

$$\mu_T = 0.00033e^{[6400/(T-1000)]} \text{Pa s}. \quad (25)$$

Here we investigate the influence of such a temperature-dependent viscosity on the dynamics, stability, and thermal evolution of a drop. For a given initial viscosity ratio, the initial magma ocean temperature is computed using (25), and we then consider an initial temperature difference with the hot metal drop of $\Delta T = 100 \text{ K}$ or $\Delta T = 1000 \text{ K}$. We focus on three reference cases, only changing

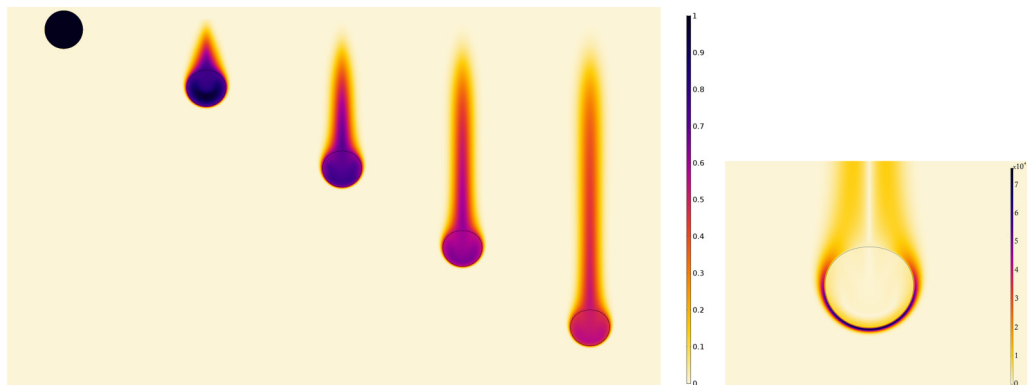


FIG. 15. Thermal evolution of the nondeformable metal drop as a function of normalized time (left). The color scale presents the temperature anomaly normalized by its initial value T^* , and the black solid line shows the surface of the metal drop. From left to right, $t^* = 0, 0.0167, 0.033, 0.05,$ and 0.067 . The right figure shows the temperature gradient (K/m) in and around the spherical drop. In this model, $Re = 0.76$, $Pe = 254$, and $R_\mu = 1000$ (simulation no. 3 in Table II).

the viscosity ratio (see Table II). Those cases are first presented in the absence of temperature-dependent viscosity:

(i) The nondeformable drop case (simulation no. 3 in Table II, $Re = 0.76$ and $Pe = 254$) is presented in Fig. 15. Drop's shape remains mostly constant. The temperature is close to uniform inside the drop because of internal recirculation and progressively decreases in the wake. Most heat transfer takes place at the front.

(ii) The weakly deformable drop case (simulation no. 5 in Table II, $Re = 21.8$ and $Pe = 728.36$) is presented in Fig. 16. The drop quickly deforms toward a spherical cap, associated with a strong release of heat in its wake. The system then reaches a quasi-steady state, with the most surprising feature being a more rapid temperature decrease in the drop than in the wake, leading to a positive heat transfer from the silicate to the iron in the drop's back. Nevertheless, most heat transfer still takes place at the front.

(iii) Finally, the strongly deformable drop case (simulation no. 6 in Table II, $Re = 47.6$ and $Pe = 793.73$) is presented in Fig. 17. Here the drop shape keeps oscillating over the whole depth because of competing surface tension and inertial forces. This induces oscillatory temperature changes in the wake, associated to periodic thermal plumes emitted from the drop sides and strong inhomogeneous fluxes within the magma ocean. Nevertheless, heat transfers between iron and silicate are still largely focused at the drop's front, explaining that this case is not associated with any specific signature in the previous section.

We now rerun those three cases using the previously defined temperature-dependent viscosity.

A. Drop dynamics

Figure 18 shows the normalized average velocity of each drop as a function of the normalized time for constant magma ocean viscosity in black lines and for temperature-dependent viscosity with $\Delta T = 100$ K ($\Delta T = 1000$ K) in red (blue) dashed lines. The normalized average velocity for the nondeformable drop (Fig. 18, left) with $\Delta T = 100$ K increases moderately by about 4.8% compared to the constant viscosity case, keeping the spherical shape without change in the morphology. For $\Delta T = 1000$ K, the drop deforms from the back side and its velocity strongly increases by about 26%; concomitantly, the average viscosity around the drop decreases by 93%, explaining this significant dynamical change. Such significant changes of the drag in the Stokes regime for an underdeformable drop were already addressed in Refs. [44,45].

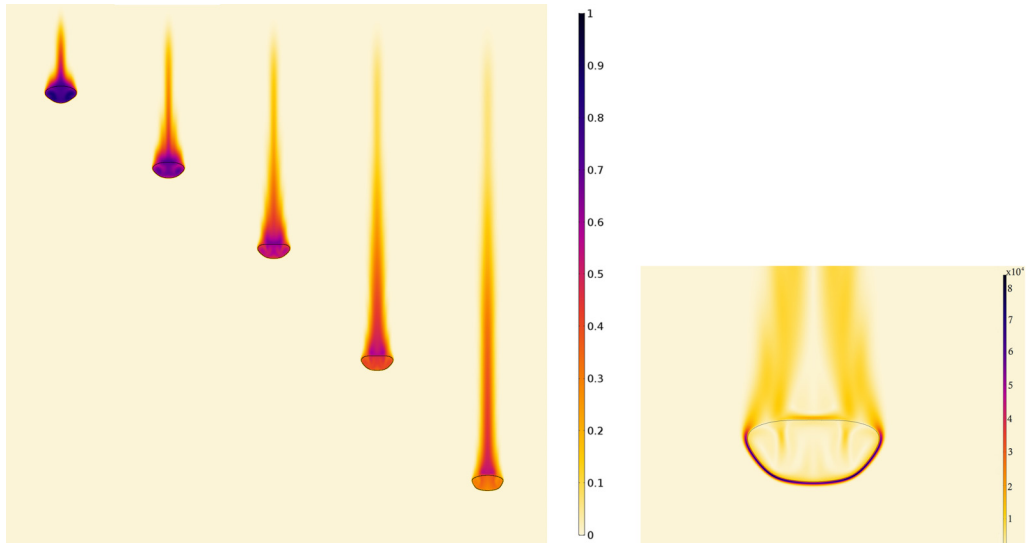


FIG. 16. Thermal evolution of the weakly deformable metal drop as a function of normalized time (left). The color scale presents the temperature anomaly normalized by its initial value T^* , and the black solid line shows the surface of the metal drop. From left to right, $t^* = 0.015, 0.024, 0.033, 0.047, \text{ and } 0.06$. The right figure shows the temperature gradient (K/m) in and around the deformable drop. In this model, $Re = 21.8$, $Pe = 728.36$, and $R_\mu = 100$ (simulation no. 5 in Table II).

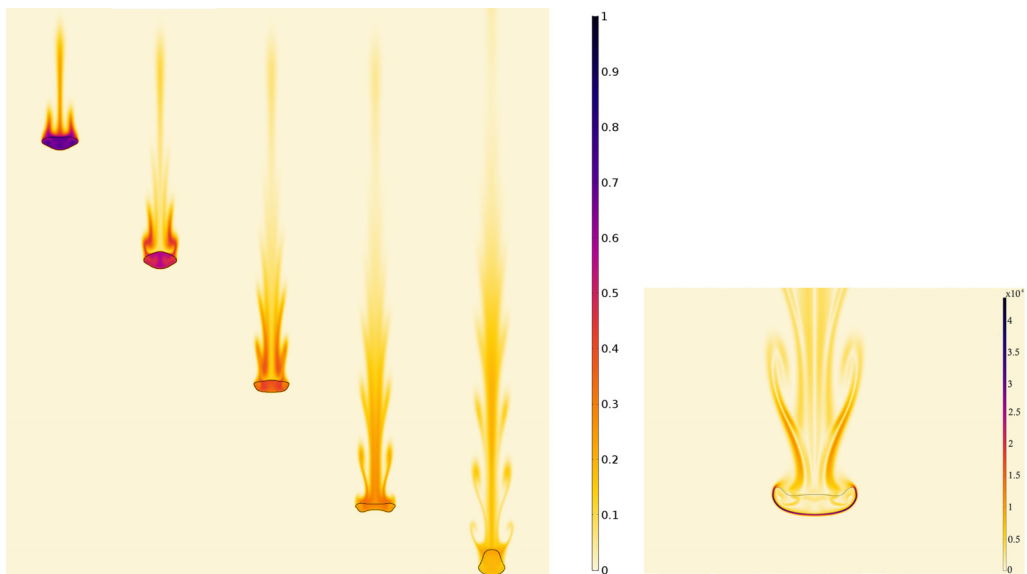


FIG. 17. Thermal evolution of the strongly deformable metal drop as a function of normalized time (left). The color scale presents the temperature anomaly normalized by its initial value T^* , and the black solid line shows the surface of the metal drop. From left to right, $t^* = 0.02, 0.033, 0.047, 0.06, \text{ and } 0.077$. The right figure shows the temperature gradient (K/m) in and around the deformable drop. In this model, $Re = 47.6$, $Pe = 793.73$, and $R_\mu = 50$ (simulation no. 6 in Table II).

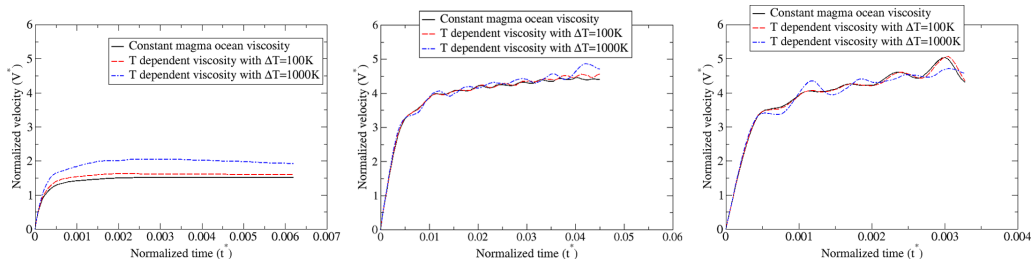


FIG. 18. Comparison of the normalized average velocity field as a function of normalized time to show the influence of a temperature-dependent viscosity for a nondeformable spherical drop (left), a weakly deformable drop (middle) and a strongly deformable drop (right). The black lines present the constant magma ocean viscosity. The red (blue) dashed lines present the temperature-dependent viscosity with $\Delta T = 100$ K ($\Delta T = 1000$ K).

On the contrary, for the weakly deformable drop (Fig. 18, middle) and the strongly deformable drop (Fig. 18, right), no significant dynamical change is observed, despite a large viscosity decrease in the associated thermal boundary layer (by 76% and 92%, respectively, for $\Delta T = 1000$ K; see also Fig. 19). This indicates that the drop dynamics is already mostly inviscid in the absence of temperature-dependent viscosity, as can be guessed from the corresponding values of the Reynolds number (see caption of Figs. 16 and 17).

B. Drop fragmentation

In the most extreme previous case (the strongly deformable drop with $\Delta T = 1000$ K), Fig. 19 indicates that the hot silicate layer surrounding the drop has a viscosity value of the order 0.05 Pa s: Assuming such a viscosity uniformly in the ambient magma ocean, our previous study [27] predicts a rapid fragmentation, which is not observed here. Actually, the viscosity contrast at the interface does not influence the drop stability, because the thermal boundary layer where the low viscosity is localized is very thin in front of the drop, compared to any relevant dynamical length scale; besides, the wake has no influence on the drop. Temperature-dependent viscosity only affects the drop's

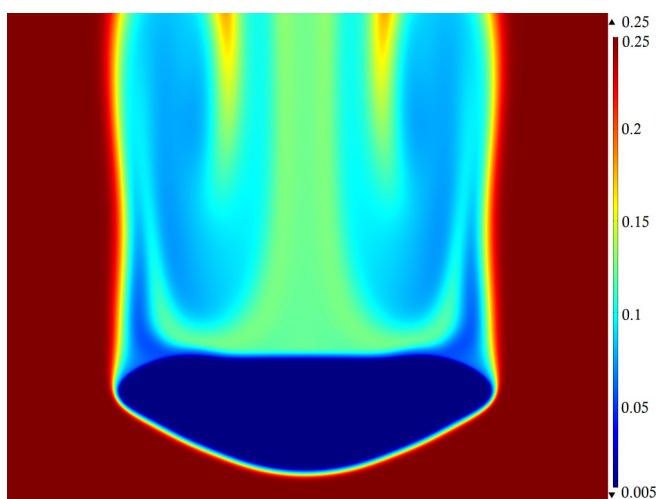


FIG. 19. View of the viscosity field (in Pa s) around the strongly deformable drop when a temperature-dependent viscosity is considered.

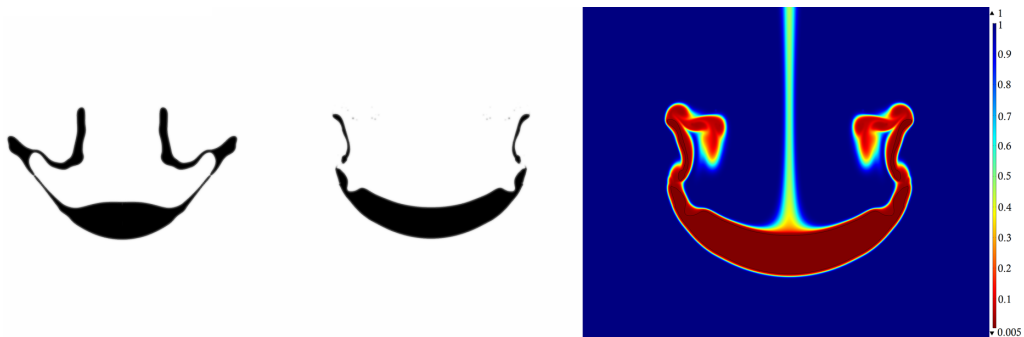


FIG. 20. Final form at breaking of the drop for a constant viscosity magma ocean (left) and a temperature-dependent viscosity magma ocean with $\Delta T = 1000$ K (middle). On the right, view of the viscosity field (in Pa.s) around the drop in the later case. In this model, $Re = 50$, $Pe = 3330$, and $R_\mu = 200$ (simulation no. 10 in Table II).

dynamics and fragmentation when flows and temperature change on comparable scales in upfront or sides locations.

To further prove this, we performed a simulation with a drop radius of 25 mm and a viscosity ratio of 200 for constant magma ocean viscosity first and then for $\Delta T = 1000$ K–dependent magma ocean viscosity (simulation no. 10 in Table II). Figure 20 (left) shows the jellyfish fragmentation mode when constant magma ocean viscosity is considered (more details can be found in Ref. [27]). The normalized time ($t_{bk}^* = \frac{t_{bk} V}{2R} \sqrt{\frac{\rho_d}{\rho_m}}$) and distance ($d_{bk}^* = \frac{d_{bk}}{R}$) of breakup equal 3.8 and 10.7, respectively. For temperature-dependent viscosity (Fig. 20, middle), another jellyfish fragmentation mode is observed, with time and distance of breakup equal to 2.3 and 5.6, respectively. Actually, here the extended jellyfish membranes form filaments, where thermal effects are very important. These membranes sink into a less-viscous medium whose thickness is comparable to the membranes thickness (see Fig. 20, right). Thus, the filaments move freely in this zone with low viscous constraints and finally separate from the drop volume, leading to fragmentation.

Note finally that the local dimensionless numbers, taken at the mean temperature (and associated viscosity) of the thermal boundary layer, become $Re = 1000$, $We = 19$, and $R_\mu = 10$. From Figs. 4, 12, and 13 of our previous study [27], we find consistent results for the fragmentation mode of the drop, as well as for its time and distance of breakup, accounting for these dimensionless numbers (to compare with our previous study, Re and We should be multiplied in this study by a factor 2 because in Ref. [27], Re and We were calculated using the drop diameter).

Hence, temperature-dependent magma ocean viscosity influences the drop fragmentation in the filament forming regimes only. In such regimes, the results in Ref. [27] as a function of Re , We , and R_μ already allow predicting fragmentation mode, breaking time and distance by considering local values of the dimensionless numbers.

C. Thermal evolution

In Fig. 21, we compare the normalized mean iron temperature for each case as a function of normalized time. For a nondeformable drop (Fig. 21, left), the average temperature for $\Delta T = 100$ K (red dashed lines) and $\Delta T = 1000$ K (blue dashed lines) temperature-dependent viscosity decreases by about 6.1% and 20.8% with respect to the constant viscosity case (black line). As a consequence, it significantly changes the characteristic time and length of equilibration (see Table III). For a weakly deformable drop (Fig. 21, middle), the average temperature evolution with $\Delta T = 1000$ K changes only by about 13.6%; no difference is measured for a strongly deformable drop (Fig. 21, right). As for the fall velocity, temperature-dependent viscosity influences significantly the thermal

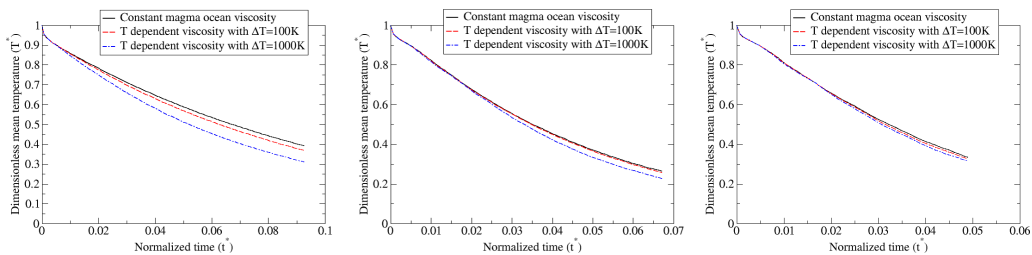


FIG. 21. Comparison of the dimensionless temperature as a function of normalized time for a nondeformable drop (left), a weakly deformable drop (middle) and a strongly deformable drop (right). The black lines present the constant magma ocean viscosity. The red (blue) dashed lines present the temperature-dependent viscosity with $\Delta T = 100$ K ($\Delta T = 1000$ K).

evolution of nondeformable drops only (i.e., the drops in the Stokes regime). Note, finally, that in the intermediate regime, the characteristics time and length of equilibration decrease slightly with a temperature-dependent viscosity compared to the constant magma ocean viscosity case, whereas in the Stokes regime, the equilibrium characteristic length increases with a temperature-dependent viscosity, in contrast to the characteristic time of equilibration (see Table III).

Regarding the volume of heated magma ocean shown in Fig. 22, no significant change is observed for all cases with $\Delta T = 100$ K (red dashed lines). The volume of heated magma ocean increases by about 1.5 to 2 times compared to the constant viscosity case (black line) for $\Delta T = 1000$ K (blue dashed lines) due to the initial larger temperature difference; but the curves remain parallel, hence exhibiting no specific dynamical signature.

Finally, we have measured the heat transfer between the two phases for all drops with a temperature-dependent viscosity. As shown in Table IV, in agreement with our previous observations, we do not notice any significant change compared to our scaling law for constant viscosity, except maybe for the less deformable drop: Indeed, heat transfer is mostly due to diffusive exchanges through a thin thermal boundary layer at the drop front, which are not affected by temperature-dependent viscosity. The same conclusion was reached experimentally in Ref. [45] in his study of diapiric magma transport through the lithosphere, hence in the limit of small Reynolds number, nondeformable drop, and using an exponential form of the temperature-dependent viscosity law. Associated numerical simulations in Ref. [44] in the limit of infinite Prandtl number exhibited a very weak dependence on the total viscosity variation. Additional systematic studies, both experimental and numerical, are necessary to explore the parameter range relevant to

TABLE III. The change in characteristics time and length for cases also studied with a temperature-dependent viscosity.

Simulation	ΔT	t_c^*	l_c^*
no. 3 (constant magma ocean viscosity)	100	0.1	24.25
no. 3a (T -dependent μ_m)	100	0.0975	25.6
no. 3b (T -dependent μ_m)	1000	0.082	27
no. 5 (constant magma ocean viscosity)	100	0.05	35.14
no. 5a (T -dependent μ_m)	100	0.0496	33.33
no. 5b (T -dependent μ_m)	1000	0.045	31.25
no. 6 (constant magma ocean viscosity)	100	0.045	32
no. 6a (T -dependent μ_m)	100	0.044	29.4
no. 6b (T -dependent μ_m)	1000	0.042	27.7

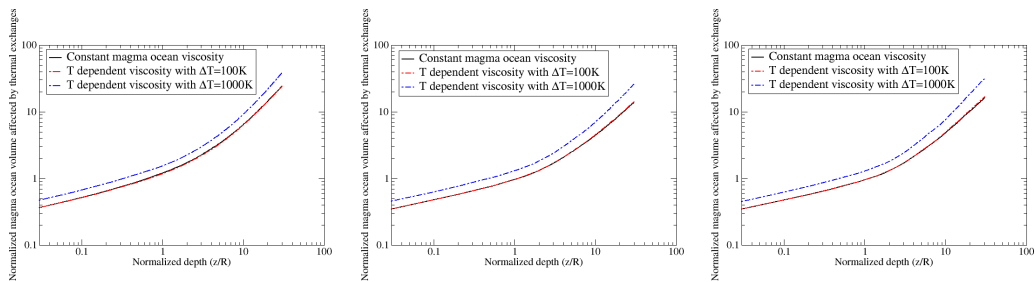


FIG. 22. Comparison of normalized heated magma ocean volume as a function of normalized time for a nondeformable drop (left), a weakly deformable drop (middle) and a strongly deformable drop (right). The black lines present the constant magma ocean viscosity. The red (blue) dashed lines present the temperature-dependent viscosity with $\Delta T = 100$ K ($\Delta T = 1000$ K).

our configuration. In the meantime, we suggest that using our scaling law [Eq. (22)] is the most acceptable solution.

VI. CONCLUSIONS AND FUTURE WORK

We have carried out series of numerical simulations to characterize the thermal exchanges between a falling drop and a viscous ambient fluid, exploring a new parameter range relevant for the geophysical application of a hot liquid iron drop falling in a magma ocean. We have shown that because of drop distortions, thermal equilibration properties slightly change from the theoretical predictions based on diffusive heat exchanges through a laminar thermal boundary layer. We have also tested that accounting for a temperature-dependent viscosity in the magma ocean barely influences the obtained results, except for limited cases like nondeformable, low-Reynolds-number drops or jellyfish fragmentation mode. Our most relevant results for geophysical application are the scaling laws for the normalized length of equilibration and for the Nusselt number, which both increase monotonically with the Peclet number as $Pe^{0.41 \pm 0.01}$ and $Pe^{0.63 \pm 0.02}$, respectively.

Future work should now consider (i) the presence of convection in the ambient magma ocean, which could affect our conclusions providing the associated velocity at the drop scale is at least of similar order as the falling drop velocity, hence requiring extremely turbulent regimes, and (ii) chemical exchanges between iron and silicates, which will determine the initial chemical state of the considered planet (see, e.g., Ref. [46]). Chemical and thermal constitutive equations being similar, similar equilibration scaling laws and dynamics are nevertheless expected.

TABLE IV. Comparison of the Nusselt numbers for cases of temperature-dependent viscosity between our numerical results and our scaling law for constant viscosity Eq. (22).

Simulation	Nu: measured	Nu: Eq. (22)	Relative error (%)
no. 3a	2.65	2.72	2.6
no. 3b	2.95	3.07	4.1
no. 5a	5.15	5.17	0.4
no. 5b	5.21	5.33	2.3
no. 6a	5.28	5.36	1.5
no. 6b	5.35	5.36	0.2

ACKNOWLEDGMENTS

The authors acknowledge funding by the European Research Council under the European Union's Horizon 2020 research and innovation program through Grant No. 681835-FLUDYCO-ERC-2015-CoG. This research also received funding from the French PNP program (INSU-CNRS), the French Government Laboratory of Excellence initiative No. ANR-10-LABX-0006, and the Région Auvergne. This paper is Laboratory of Excellence ClerVolc Contribution No. 406. We are grateful to the Mésocentre Clermont Auvergne University for providing help as well as computing and storage resources.

-
- [1] T. Kleine, C. Münker, K. Mezger, and H. Palme, Rapid accretion and early core formation on asteroids and the terrestrial planets from Hf-W chronometry, *Nature* **418**, 952 (2002).
 - [2] M. Touboul, T. Kleine, B. Bourdon, H. Palme, and R. Wieler, Late formation and prolonged differentiation of the Moon inferred from W isotopes in lunar metals, *Nature* **450**, 1206 (2007).
 - [3] R. Deguen, P. Olson, and P. Cardin, Experiments on turbulent metal-silicate mixing in a magma ocean, *Earth Planet. Sci. Lett.* **310**, 303 (2011).
 - [4] R. Deguen, M. Landeau, and P. Olson, Turbulent metal-silicate mixing, fragmentation, and equilibration in magma oceans, *Earth Planet. Sci. Lett.* **391**, 274 (2014).
 - [5] M. Landeau, R. Deguen, and P. Olson, Experiments on the fragmentation of a buoyant liquid volume in another liquid, *Fluid Mech.* **749**, 478 (2014).
 - [6] D. J. Stevenson, Fluid dynamics of core formation, *Origin of the Earth* (Oxford University Press, 1990), pp. 231–249.
 - [7] J. B. Wacheul and M. Le Bars, Experiments on fragmentation and thermo-chemical exchanges during planetary core formation, *Phys. Earth Planet. Int.* **276**, 134 (2018).
 - [8] J. B. Wacheul, M. LeBars, J. Monteux, and J. M. Aurnou, Laboratory experiments on the breakup of liquid metal diapirs, *Earth Planet. Sci. Lett.* **403**, 236 (2014).
 - [9] W. K. Hartmann and D. R. Davis, Satellite-sized planetesimals and lunar origin, *Icarus* **24**, 504 (1975).
 - [10] J. Monteux, N. Coltice, F. Dubuffet, and Y. Ricard, Thermo-mechanical adjustment after impacts during planetary growth, *Geophys. Res. Lett.* **34**, 24201 (2007).
 - [11] W. B. Tonks and H. J. Melosh, Core formation by giant impacts, *Icarus* **100**, 326 (1992).
 - [12] M. J. Walter and R. G. Tronnes, Early earth differentiation, *Earth Planet. Sci. Lett.* **225**, 253 (2004).
 - [13] J. Monteux, Y. Ricard, N. Coltice, F. Dubuffet, and M. Ulvrova, A model of metal-silicate separation on growing planets, *Earth Planet. Sci. Lett.* **287**, 353 (2009).
 - [14] H. Genda, R. Brasser, and S. J. Mojzsis, The terrestrial late veneer from core disruption of a lunar-sized impactor, *Earth Planet. Sci. Lett.* **480**, 25 (2017).
 - [15] J. D. Kendall and H. Melosh, Differentiated planetesimal impacts in a terrestrial magma ocean: Fate of the iron core, *Earth Planet. Sci. Lett.* **448**, 24 (2016).
 - [16] H. Ichikawa, S. Labrosse, and K. Kurita, Direct numerical simulation of an iron rain in the magma ocean, *Geophys. Res.* **115**, B01404 (2010).
 - [17] D. C. Rubie, H. J. Melosh, J. E. Reid, C. Liebske, and K. Righter, Mechanisms of metal-silicate equilibration in the terrestrial magma ocean, *Earth Planet. Sci. Lett.* **205**, 239 (2003).
 - [18] H. Samuel, A re-evaluation of metal diapir breakup and equilibration in terrestrial magma oceans, *Earth Planet. Sci. Lett.* **313–314**, 105 (2012).
 - [19] T. W. Dahl and J. Stevenson, Turbulent mixing of metal and silicate during planet accretion and interpretation of the hf-w chronometer, *Earth Planet. Sci. Lett.* **295**, 177 (2010).
 - [20] M. Ulvrova, N. Coltice, Y. Ricard, S. Labrosse, F. Dubuffet, J. Velimský, and M. Šrámek, Compositional and thermal equilibration of particles, drops, and diapirs in geophysical flows, *Geochem. Geophys. Geosyst* **12**, Q10014 (2011).
 - [21] B. B. Karki and L. P. Stixrude, Viscosity of mgsio₃ liquid at earth's mantle conditions: Implications for an early magma ocean, *Science* **328**, 740 (2010).

- [22] T. Bonometti and J. Magnaudet, Transition from spherical cap to toroidal bubbles, *Phys. Fluids* **18**, 052102 (2006).
- [23] M. Ohta and M. Sussman, The buoyancy-driven motion of a single skirted bubble or drop rising through a viscous liquid, *Phys. Fluids* **24**, 112101 (2012).
- [24] M. Ohta, Y. Akama, Y. Yoshida, and M. Sussman, Three-dimensional simulations of vortex ring formation from falling drops in an immiscible viscous liquid, *Chem. Eng. Jpn.* **42**, 648 (2009).
- [25] M. Ohta, S. Yamaguchi, Y. Yoshida, and M. Sussman, The sensitivity of drop motion due to the density and viscosity ratio, *Phys. Fluids* **22**, 072102 (2010).
- [26] M. Ohta, Y. Akama, Y. Yoshida, and M. Sussman, Influence of the viscosity ratio on drop dynamics and breakup for a drop rising in an immiscible low-viscosity liquid, *Fluid Mech.* **752**, 38 (2014).
- [27] B. Qaddah, J. Montoux, V. Clesi, A. Bouhifd, and M. Le Bars, Dynamics and stability of an iron drop falling in a magma ocean, *Phys. Earth Planet. Int.* **289**, 75 (2019).
- [28] H. Samuel, P. J. Tackley, and M. Evonuk, Heat partitioning in terrestrial planets during core formation by negative diapirism, *Earth Planet. Sci. Lett.* **290**, 13 (2010).
- [29] F. M. Flasar and F. Birch, Energetics of core formation: A correction, *J. Geophys. Res.* **78**, 6101 (1973).
- [30] X-Y. Luo, M.-J. Ni, A. Ying, and M. Abdou, Application of the level set method for multi-phase flow computation in fusion engineering, *Fus. Eng. Des.* **81**, 1521 (2006).
- [31] J. Hu, R. Jia, K. T. Wan, and X. Xiong, Simulation of droplet impingement on a solid surface by the level set method, in *Proceedings of the COMSOL Conference in Boston* (COMSOL, Boston, 2014).
- [32] V. Lherm and R. Deguen, Small-scale metal/silicate equilibration during core formation: The influence of stretching enhanced diffusion on mixing, *J. Geophys. Res.: Solid Earth* **123**, 10,496 (2018).
- [33] D. C. Rubie, F. Nimmo, and H. J. Melosh, *Formation of the Earth's Core, Treatise on Geophysics – Evolution of the Earth* (2nd ed.) (Elsevier, Amsterdam, 2015), pp. 43–79.
- [34] A. M. Hofmeister, Mantle values of thermal conductivity and the geotherm from phonon lifetimes, *Science* **283**, 1699 (1999).
- [35] C. W. Thomas and P. D. Asimow, Direct shock compression experiments on premolten forsterite and progress toward a consistent high-pressure equation of state for cao-mgo-al2o3-sio2-feo liquids, *J. Geophys. Res.: Solid Earth* **118**, 5738 (2013).
- [36] N. de Koker, G. Steinle-Neumann, and V. Vlček, Electrical resistivity and thermal conductivity of liquid fe alloys at high p and t, and heat flux in earth's core, *Proc. Natl. Acad. Sci. USA* **109**, 4070 (2012).
- [37] H. Ichikawa, T. Tsuchiya, and Y. Tange, The p-v-t equation of state and thermodynamic properties of liquid iron, *J. Geophys. Res.: Solid Earth* **119**, 240 (2014).
- [38] M. Pilch and C. A. Erdman, Use of breakup time data and velocity history data to predict the maximum size of stable fragments for acceleration-induced breakup of a liquid drop, *Multiphase Flow* **13**, 741 (1987).
- [39] E. Villermaux and B. Bossa, Single-drop fragmentation determines size distribution of rain drops, *Nat. Phys.* **5**, 697 (2009).
- [40] S. S. Jain, N. Tyagi, R. S. Prakash, R. V. Ravikrishna, and G. Tomar, Secondary breakup of drops at moderate Weber numbers: Effect of Density ratio and Reynolds number, *Int. J. Multiphase Flow* **117**, 25 (2019).
- [41] J. Crank, *The Mathematics of Diffusion* (2nd ed.) (Clarendon Press, Oxford, 1975).
- [42] R. C. Mittal and R. K. Jain, Redefined cubic b-splines collocation method for solving convection–diffusion equations, *Appl. Math. Model.* **36**, 5555 (2012).
- [43] J. R. Fleck, C. L. Rains, D. S. Weeraratne, C. T. Nguyen, D. M. Brand, S. M. Klein, J. M. McGehee, J. M. Rincon, C. Martinez, and P. L. Olson, Iron diapirs entrain silicates to the core and initiate thermochemical plumes, *Nat. Commun.* **9**, 71 (2018).
- [44] S. F. Daly and A. Raefsky, On the penetration of a hot diapir through a strongly temperature-dependent viscosity medium, *Geophys. J. Int.* **83**, 657 (1985).
- [45] N. M. Ribe, Diapirism in the earth's mantle: Experiments on the motion of a hot sphere in a fluid with temperature-dependent viscosity, *J. Volcanol. Geotherm. Res.* **16**, 221 (1983).
- [46] M. Bouhifd and A. Jephcoat, The effect of pressure on partitioning of ni and co between silicate and iron-rich metal liquids: A diamond-anvil cell study, *Earth Planet. Sci. Lett.* **209**, 245 (2003).